Mon. Not. R. Astron. Soc. **377,** 883–896 (2007) doi:10.1111/j.1365-2966.2007.11658.x

The shape of galaxy cluster dark matter haloes: systematics of its imprint on cluster gas and comparison to observations

Ricardo A. Flores,[1⋆] Brandon Allgood,[2⋆] Andrey V. Kravtsov,[3⋆] Joel R. Primack,[4⋆] David A. Buote[5⋆] and James S. Bullock[6⋆]

[1]*Department of Physics and Astronomy, University of Missouri – St Louis, St Louis, MO 63121, USA*
[2]*Physics Department, University of California, Santa Cruz, CA 95064, USA*
[3]*Department of Astronomy and Astrophysics, Kavli Institute for Cosmological Physics, and The Enrico Fermi Institute, The University of Chicago, Chicago IL 60637, USA*
[4]*Physics Department, University of California, Santa Cruz, CA 95064, USA*
[5]*Department of Physics and Astronomy, University of California, Irvine, CA 92697, USA*
[6]*Center for Cosmology, Department of Physics and Astronomy, University of California, Irvine, CA 92697, USA*

Accepted 2007 February 21. Received 2006 December 20; in original form 2005 September 2

ABSTRACT

We study predictions for galaxy cluster observables that can test the statistics of dark matter halo shapes expected in a flat Λ cold dark matter (CDM) universe. We present a simple analytical model for the prediction of cluster-scale X-ray observations, approximating clusters as isothermal systems in hydrostatic equilibrium, and dark matter haloes as ellipsoids with uniform axial ratios (homeoidal ellipsoids). We test the model against high-resolution, hydrodynamic cluster simulations to gauge its reliability. We find that this simple prescription does a good job of predicting cluster X-ray ellipticities compared to the simulations as long as one focuses on cluster regions that are less sensitive to recent mergers. Based on this simple model, the distribution of cluster-size halo shapes expected in the concordance ΛCDM cosmology implies an X-ray ellipticity distribution with a mean $\langle\epsilon_{\rm X}\rangle = 0.32 \pm 0.01$, and a scatter $\sigma_\epsilon = 0.14 \pm 0.01$ for the mass range $(1\text{–}4) \times 10^{14}\, h^{-1}\, {\rm M}_\odot$. We find it important to include the mass dependence of halo shape when making comparisons to observational samples. We analyse the systematics of four observational samples of cluster ellipticities and find that our results are statistically compatible with these observations. In particular, we find remarkably good agreement between two recent *ROSAT* samples and ΛCDM predictions that *do not* include gas cooling. We also test how well our analytical model can predict Sunyaev–Zel'dovich decrement maps and find that it is less successful although still useful; the model does not perform as well as a function of flux level in this case because of the changing triaxiality of dark matter haloes as a function of radial distance. Both this effect and the changing alignment of isodensity shells of dark matter haloes leave an imprint on cluster gas that appears to be seen in observational data. Thus, dark matter haloes cannot be accurately characterized as homeoidal ellipsoids for all comparisons.

Key words: cosmology: theory – dark matter – X-rays: galaxies: clusters.

1 INTRODUCTION

Clusters of galaxies are the largest bound structures in the Universe and the most recently formed ones according to the very successful cold dark matter (CDM) cosmology. As such, their dark matter (DM) haloes are expected to be less evolved and more aspherical than, say, galaxy-size haloes. Most gas in cluster DM haloes has not had time to cool, and since it is gravitationally subdominant, we can expect it to reflect the underlying 3D shape of their dark matter haloes. Indeed, large samples of X-ray clusters have been known to show a broad distribution of ellipticities in their surface brightness (SB) maps since the work of McMillan, Kowalski & Ulmer (1989). A comparison of theoretical predictions to such observations, now that basic parameters of the underlying cosmology are known at the 10 per cent level or better, may shed light on the basic description of the gas in clusters of galaxies.

The general expectation that in CDM-based theories DM haloes are flattened, are approximately ellipsoidal and have short-to-long axial ratios as small as $s \equiv c/a \sim 0.5$ has been known for more

⋆E-mail: ricardo.flores@umsl.edu (RAF); allgood@physics.ucsc.edu (BA); andrey@oddjob.uchicago.edu (AVK); joel@scipp.ucsc.edu (JRP); buote@uci.edu (DAB); bullock@uci.edu (JSB)

than 15 yr now (Barnes & Efstathiou 1987; Frenk et al. 1988). Any asphericity in the DM distribution has important effects on a variety of observed quantities. In clusters in particular, asphericity in the dark halo potential will map directly to asphericity in the gas density, and thus affect the shape of cluster X-ray isophotes and Sunyaev–Zel'dovich (SZ) isodecrement contours. Much subsequent work since these pioneering studies aimed at understanding the influence of the cosmological model on axial ratios, and improving the resolution with which the formation of DM haloes was followed (Dubinski & Carlberg 1991; Warren et al. 1992; Jing et al. 1995; Thomas et al. 1998; Suwa et al. 2003).

Recently, higher resolution dissipationless simulations have made it possible *to fully characterize the scatter and mean of axial ratios*, as a function of both mass and epoch (Bullock 2002; Jing & Suto 2002, hereafter JS; Kasun & Evrard 2005; Allgood et al. 2006, hereafter Paper I). JS calculated for the first time axial ratios for isodensity shells, using cosmological simulations with 512^3 particles. They confirmed that haloes are approximately ellipsoidal in isodensity contours and have provided fits for the dependence of axial ratios on mass and epoch. Because the isodensity contour method requires a large number of particles, JS restricted their analysis to haloes more massive than $6.2 \times 10^{12}\,h^{-1}\,\mathrm{M}_{\odot}$ in their ΛCDM simulation. Kasun & Evrard (2005) have obtained better statistics for haloes more massive than $3 \times 10^{14}\,h^{-1}\,\mathrm{M}_{\odot}$ from a Hubble volume simulation. We (Paper I) have studied haloes spanning the mass range 4×10^{11}–$2 \times 10^{14}\,h^{-1}\,\mathrm{M}_{\odot}$ using several simulations to properly resolve and adequately sample the halo population in this entire mass range. The results (extrapolated) agree with results of the Millennium Simulation for 100 haloes of average mass $2 \times 10^{15}\,h^{-1}\,\mathrm{M}_{\odot}$ (Eric Hayashi, private communication). The results are consistent with those of JS for haloes of low-mass clusters, but yield a steeper mass dependence of axial ratios than a simple extrapolation of the scaling relations found by JS. This difference is important in the interpretation of observations on galaxy scales (Paper I) and, as we show here (Section 3), in the interpretation of X-ray ellipticities of samples containing very massive clusters. Our results are in agreement with those of Kasun & Evrard (2005) if axial ratios are calculated in the same manner. However, we find here that axial ratios calculated that way are not useful for predictions of cluster observables such as X-ray or SZ maps (see Appendix A).

A source of uncertainty in the current understanding of halo shapes is the magnitude of the effect of gas cooling on cluster DM haloes. Here, we find good agreement between the distribution of ellipticities extracted from two *ROSAT* samples and the distribution predicted from ΛCDM simulations that do not include gas cooling. This is surprising in view of the results from simulations that include cooling and star formation, which find DM haloes significantly rounder, especially near the centre (Kazantzidis et al. 2004; Springel, White & Hernquist 2004). Cooling and star formation must certainly occur. However, our results could be indicative that other energy input is at work that balances out radiative cooling. Indeed, it has been known for many years that the presence of hot gas in cluster cores (inside 100 kpc) with radiative cooling time-scales much shorter than the Hubble time leads to the expectation of massive cooling flows of hundreds of $\mathrm{M}_{\odot}\,\mathrm{yr}^{-1}$. However, *Chandra* and *XMM–Newton* observations now indicate much smaller rates (for a review see Fabian 2003). Thus, a mechanism to balance out cooling is needed. Heating by active galactic nuclei (AGN) appears to be a mechanism powerful enough to balance cooling (see Heinz et al. 2006, and references therein). Conduction is another potential mechanism, perhaps allowing enough transport of heat to balance cooling in some cases (see Zakamska & Narayan 2003, and references therein). Yet another argument for energy input into the intracluster medium, needed out to larger radii, comes from the steep luminosity–temperature relation observed in clusters, which could also be accounted for by AGN heating (for a recent discussion see Begelman & Ruszkowski 2005, and references therein).

The variety of current and future observational probes of halo ellipticity (see Paper I for a discussion) highlights the need to connect these predictions to observations in a robust fashion. Very high mass resolution hydrodynamical simulations on large enough scales to yield a large statistical sample of clusters would be ideal to make the connection. However, the high mass resolution is available on such scales only without hydrodynamics, or available with hydrodynamics for several clusters simulated individually on a smaller scale. Another avenue is to explore models that would allow predictions to be made for cluster X-ray or SZ ellipticities based on the 3D shape of their DM haloes, whose shape statistics can be accurately characterized (see Paper I). A perturbative model has been developed by Lee & Suto (2003), and further extended by Wang & Fan (2004) to predict observed distributions from halo shape distributions, but it is not useful for our purposes here because the ellipticities can be quite large.

Here, we present an analytic method for predicting gravitational potentials and cluster gas density based on axial ratios of dark matter haloes. We test the model against a sample of eight high-resolution hydrodynamic Adaptive Refinement Tree (ART) simulations of seven clusters [mass $(1\text{–}2) \times 10^{14}\,h^{-1}\,\mathrm{M}_{\odot}$] and one group (mass $7 \times 10^{13}\,h^{-1}\,\mathrm{M}_{\odot}$) in the ΛCDM cosmology (Kazantzidis et al. 2004), whose highly variant morphology dependence on the line-of-sight (LOS) we exploit to statistically test the model, using also two additional clusters from earlier high-resolution hydrodynamic simulations (Kravtsov, Klypin & Hoffman 2002; Nagai & Kravtsov 2003). We find that the analytic model can be used to make fairly robust predictions for the expected distribution of ellipticities (mean and scatter).

Our paper is organized as follows. In the next section, we discuss the analytic model we use to predict cluster X-ray and SZ morphologies, and we test it by comparing predictions for morphology of the simulation clusters (based on their DM haloes only) with the same observable computed directly from the gas density grid of the hydrodynamic simulations. Then in Section 3, we focus on observations and compare our predictions to several observational samples of cluster X-ray ellipticities. We also discuss recent papers (e.g. Floor et al. 2003; Floor, Melott & Motl 2004) that have compared observed cluster shapes measured using X-rays and galaxy distributions to hydrodynamic simulations. Finally, we present in Section 4 a summary of our conclusions. The details of the comparison techniques used in Section 3 are outlined in three Appendices: (A) Gas Density Inside Triaxial Haloes; (B) Analytic Potential of Triaxial Generalized NFW Haloes and (C) A Comparison of X-ray Ellipticity Measures.

2 COMPARISON OF MODEL AND SIMULATION STATISTICS

In this section, we analyse the prediction for two statistics of cluster morphology, the mean and the dispersion of their ellipticity distribution, expected in a flat ΛCDM universe with $\Omega_{\mathrm{m}} = 0.3$, $h = 0.7$ and $\sigma_8 = 0.9$. We first discuss the method to predict cluster ellipticities based on their dark matter haloes and then present the comparison of the predictions to the results from the output of several

high-resolution hydrodynamical simulations (Kazantzidis et al. 2004). In what follows, the virial radius is defined as the radius, $r_{\rm vir}$, within which the mean overdensity drops to $\Delta = 18\pi^2 + 82[\Omega_{\rm m}(z) - 1] - 39[\Omega_{\rm m}(z) - 1]^2$ (Bryan & Norman 1998). Masses are defined as the mass within $r_{\rm vir}$.

2.1 Method

We use a diagonalized moment of inertia tensor iteratively calculated within ellipsoids, or ellipsoidal shells, to define axial ratios for dark matter haloes (Dubinski & Carlberg 1991). Axial ratios $s = c/a$ and $q = b/a$ ($s < q < 1$) are calculated by diagonalizing the tensor

$$\boldsymbol{M}_{ij} \equiv \Sigma \frac{x_i x_j}{R^2};\ R = \sqrt{x^2 + y^2/q^2 + z^2/s^2}, \tag{1}$$

thereby determining s and q for the next iteration. The sum is over all particles within a given shell $[R, R + \Delta R]$, or the ellipsoid interior to R, and the iteration starts with $s = q = 1$. In Paper I, we have found that this method predicts axial rations that agree with the results of JS, which are based on isodensity shells, for cluster-size haloes, provided that the axial ratios be calculated within an ellipsoid of semimajor axis $R = 0.3r_{\rm vir}$. Here, we also find that the same axial ratios can be used to predict fairly accurately the mean and dispersion of the expected X-ray ellipticities, even though as often as half the time the predicted ellipticity of an individual cluster is off by more than 20 per cent.

The X-ray SB of an isothermal cluster is given by an integral along the LOS to a cluster of the gas density squared, SB $\propto \int \rho_{\rm gas}^2 \sqrt{T}\, {\rm d}x_{\rm LOS}$. As discussed in Appendix A, under the assumptions of hydrostatic equilibrium and isothermality, the gas density at any point inside a triaxial homeoidal halo can be written in terms of the temperature T, the central gas density and the halo potential at the desired point (equation A1). If we assume that the halo potential is dominated by the dark matter, then the relation is simplified by the fact that the potential of any triaxial generalized NFW (Navarro, Frenk & White 1996) halo is analytic (Appendix B). Thus, using the relation (A1), we can estimate the X-ray ellipticities implied by a dark matter halo given the halo axial ratios and its orientation.

The only (slight) ambiguity in relating the gas density to the halo potential is the factor Γ in equation (A1), which relates the gas density to the potential exponentially: $\rho_{\rm gas} \propto \exp(-\Gamma\Phi)$. In Appendix C, we find that the analytic model works relatively well with $\Gamma \sim c_{\rm vir}$ when we compare to two high-resolution clusters. This is roughly expected for a NFW halo since

$$\Gamma \simeq sq\rho_{\rm s}R_{\rm s}^2 \frac{G\mu m_p}{kT} \simeq \frac{\sigma^{-2} G M_{\rm vir}}{r_{\rm vir}\, f(c_{\rm vir})}\, c_{\rm vir} \sim c_{\rm vir}, \tag{2}$$

where $f(x) = \ln(1 + x) - x/(1 + x)$ and σ is the LOS velocity dispersion. In the second step, we have used $sq\rho_{\rm s}R_{\rm s}^2 \simeq \rho_{\rm sph} r_{\rm s}^2$, where $\rho_{\rm sph}$ and $r_{\rm s}$ are spherical-NFW-fit parameters for the halo, and assumed the expected energy scaling, $kT \simeq \mu m_p \sigma^2$, which is even seen observationally [see e.g. Rosati, Borgani & Norman (2002) and references therein], albeit with a fair amount of scatter. The final step follows from rough scaling relations (see Appendix A), and works in detail for the clusters we consider in Appendix C. Therefore, for our comparisons we assume

$$\frac{G M_{\rm vir} \mu m_p}{r_{\rm vir}\, f(c_{\rm vir}) kT} = 1, \tag{3}$$

and use $\Gamma = c_{\rm vir}$. For the dark matter halo of the standard CDM (hereafter SCDM) (ΛCDM) cluster, we find a value of 1.06 (0.98) for the RHS of this equation, using the average temperature of the gas inside a radius of $400\,h^{-1}$ kpc.

2.2 Results

For a given dark matter halo, the method discussed above allows us to compute the SB map expected for a given LOS through that halo. We discuss in Appendix C how an X-ray ellipticity can be obtained from the SB map. There is no unique method to calculate ellipticities and, as we discuss below and in Appendix C, it is important to follow the procedure chosen by observers to calculate ellipticities in order to compare to observations. *Individual* ellipticities can differ *substantially* depending on what part of a map the procedure selects and, as we show below, *even the means* (of samples of ellipticities calculated with different procedures) *will differ*.

Fig. 1 shows SB maps for one of eight high-resolution *adiabatic* hydrodynamic simulations of clusters in the ΛCDM cosmology (see Kazantzidis et al. 2004). (Such simulations include neither radiation nor energy input to the gas, for example, from supernovae.) Each map corresponds to a LOS parallel to each of the coordinate axes of the simulation box containing the cluster (maps for all eight clusters are included as Supplementary Material to the online version of this article). We calculate the SB for a given 'pixel' in each box by summing $\rho_{\rm gas}^2\sqrt{T}$ over all cells along the LOS-axis. Each cell is $7.8\,h^{-1}$ kpc on the side and each map covers $2\,h^{-1}$ Mpc on the side. The X-ray ellipticity, $\epsilon_{\rm X}$, shown in the upper right corner of

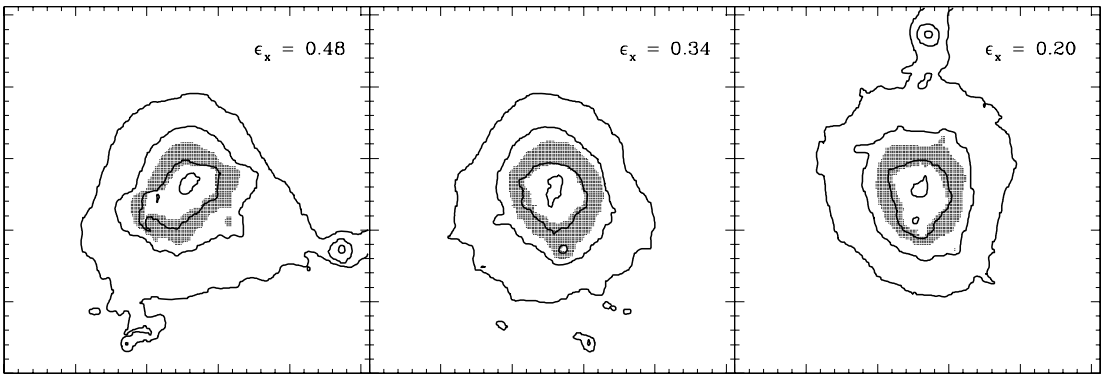

Figure 1. Sample of X-ray SB maps for one hydrodynamic simulation cluster. Each map presents the SB for a LOS along each of the axes of the simulation box. Each square is $2\,h^{-1}$ Mpc across. The solid lines show contours of constant SB, spaced by factors of 10. The shaded area is the region used to calculate the ellipticity shown in the upper right corners (see text for discussion, and the Supplementary Material section for details of the full figure).

each map, is calculated using the pixels (shown by the shaded areas) containing 20 per cent of the total flux above a threshold flux that is 1 per cent of the peak flux of the map. This is one of the procedures we consider in this work to calculate ellipticities from a SB map. It is a method that in the absence of noise yields ellipticities that reflect the potential of the DM halo, as we show in the next paragraph. McMillan et al. (1989) used this method in their study of X-ray ellipticities. However, we find below (see Section 3) that their data are heavily affected by noise and do not serve as a test of the ΛCDM cosmology. A more detailed discussion of methodologies is presented in Appendix C.

For each cluster halo, we can use the method described in Section 2.1 to compute the predicted SB map for a given LOS through the cluster, based only on its dark matter halo. We can then compute the predicted X-ray ellipticity in exactly the same manner as we compute the ellipticity for the corresponding hydrodynamic SB map (e.g. Fig. 1). In the following three figures, we show comparisons between ellipticities calculated for the eight clusters in each of the orientations of the LOS. In Fig. 2, we show a comparison between ellipticities calculated using the analytic model and calculated directly from the hydrodynamic SB maps using the method of McMillan et al. (1989). This comparison validates the model for this kind of ellipticity. Since the methodology to calculate X-ray ellipticities is not unique, in Figs 3 and 4 we explore whether the model could also be used to predict X-ray ellipticities calculated with the method used in each of the two other observational samples we consider here.

In Fig. 2, each point in the figure plots the ellipticity obtained directly from a hydrodynamic SB map (abscissa) against the ellipticity calculated based only on the DM halo parameters (ordinate). A Kolmogorov–Smirnov (KS) test gives high probability

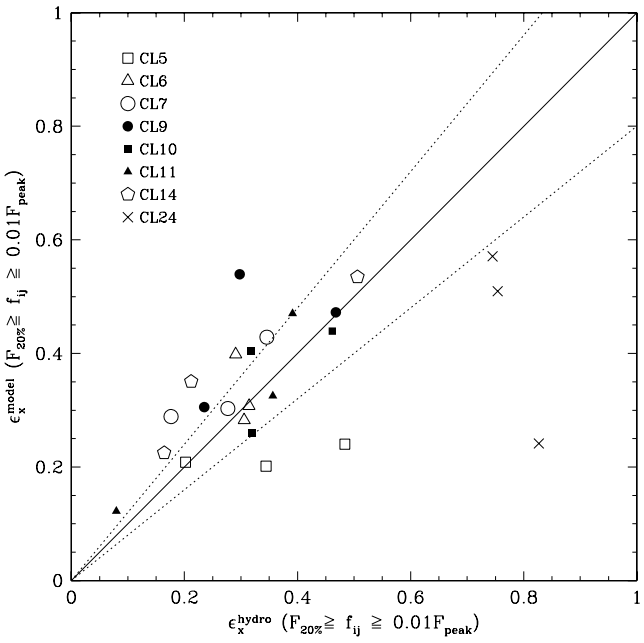

Figure 2. Comparison of X-ray ellipticities calculated with the method of McMillan et al. (1989), obtained using our analytic model (ordinate), and directly from the SB maps for the eight hydrodynamic simulation clusters. Each symbol identifies a cluster, and for each cluster the symbol plots the ellipticity calculated from the simulation map (one for a LOS along each of the coordinate axes) against the predicted ellipticity using the method described in Section 2.1. Within the dotted lines, the ellipticities differ by less than 20 per cent.

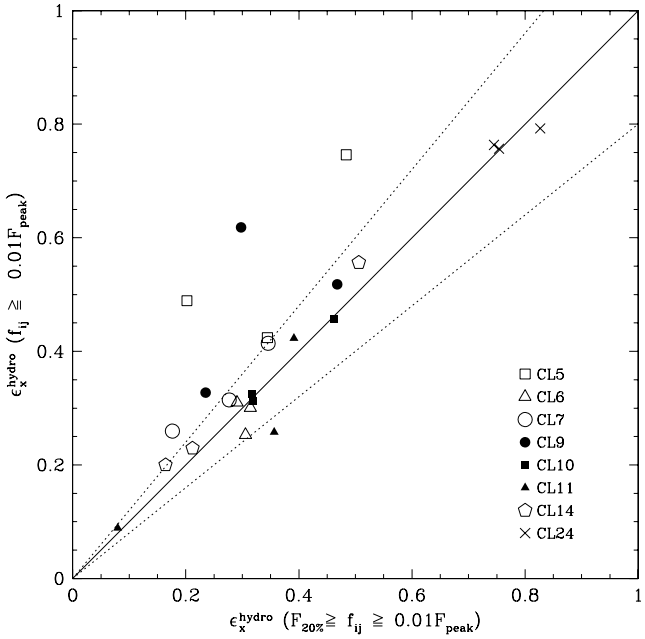

Figure 3. Comparison of ellipticities calculated directly from SB maps of the hydrodynamic simulation clusters using different strategies. The abscissa is the same as in Fig. 2. The ordinate is an ellipticity calculated using *all* pixels above a given flux threshold, in this case 1 per cent of the peak flux in a map (the method of Kolokotronis et al. 2001). Within the dotted lines, the ellipticities differ by less than 20 per cent (see text for further discussion).

($P_{KS} = 99$ per cent) that the two sets represent the same distribution. We treat the value of ϵ_X for each LOS as an independent measurement because for a given axial ratio s there is quite a degree of variability expected for the other axial ratio, and then there is the variation introduced by the orientation of the cluster to the LOS. The means of the sets indeed agree quite well: $\langle\epsilon_X^{hydro}\rangle = 0.36$, whereas $\langle\epsilon_X^{model}\rangle = 0.35$. However, the dispersions differ significantly: $\sigma_\epsilon^{hydro} = 0.18$, whereas $\sigma_\epsilon^{model} = 0.12$. This is partly due to one hydrodynamic SB map whose ellipticity is significantly enhanced by a secondary lump that has a significant relative weight due to the fact that the flux levels select a narrow region of the main cluster. Without that map, $\langle\epsilon_X^{hydro}\rangle = 0.34$, and $\sigma_\epsilon^{hydro} = 0.15$ (recalculating the ellipticity without the lump, $\langle\epsilon_X^{hydro}\rangle = 0.35$ and $\sigma_\epsilon^{hydro} = 0.15$). The remaining difference between $\sigma_\epsilon^{hydro} = 0.15$ and $\sigma_\epsilon^{model} = 0.12$ seems to be due to the fact that the gas reflects the changing triaxiality in the inner region of DM haloes. We tested this by recalculating ϵ_X^{model} using axial ratios for the DM haloes calculated within $R = 0.15r_{vir}$, in which case we find $\langle\epsilon_X^{model}\rangle = 0.35$ and $\sigma_\epsilon^{model} = 0.15$.

Thus, the analytic model can be used to make fairly robust predictions of average X-ray ellipticities. An equally robust prediction of the expected scatter does not seem possible with a simple homeoidal model of DM haloes, but its reliability might be checked by calculating two sets of ellipticities based on DM halo axial ratios calculated within two different radii. We have used the model, then, to calculate the mean and dispersion of X-ray ellipticities expected in a ΛCDM universe at the present epoch. We use a sample of 46 DM haloes extracted from the $120\,h^{-1}$ Mpc dissipationless cosmological simulation discussed in Paper I. The cosmology is a flat ΛCDM universe with $\Omega_m = 0.3, h = 0.7$ and $\sigma_8 = 0.9$ and the simulation followed 512^3 particles of mass $1.1 \times 10^9\,h^{-1}\,M_\odot$. All haloes with virial mass $(1-4) \times 10^{14}\,h^{-1}\,M_\odot$ were selected. We calculate their axial ratios and concentrations in order to predict X-ray ellipticities

for a LOS corresponding to each of the coordinate axes of the box. The ellipticity is computed as described above using two flux levels. The samples corresponding to each LOS agree quite well with each other. For the combined sample, we find

$$\langle \epsilon_{\rm X} \rangle = 0.323 \pm 0.013;\ \sigma_\epsilon = 0.138 \pm 0.008, \quad (4)$$

where the errors are calculated by bootstrap resampling. These results are consistent with those for the hydrodynamic simulation clusters, for which $\langle \epsilon_{\rm X} \rangle = 0.338 \pm 0.032$ and $\sigma_\epsilon = 0.148 \pm 0.030$.

The strategy to extract an X-ray ellipticity from a SB map is by no means unique, and in Figs 3 and 4 we present two other cases of interest here. For example, in Section 3 we discuss a sample of X-ray ellipticities obtained by Kolokotronis et al. (2001) who use a strategy that emphasizes the central region of a cluster (they were interested in mergers). In Fig. 3, we show a comparison of ellipticities (all calculated directly from the hydrodynamic simulation maps) using two different strategies. The ordinate is an ellipticity very similar to that of Kolokotronis et al. (2001), calculated using all pixels above a flux threshold corresponding to 1 per cent of the peak flux of the SB map. The abscissa is as in Fig. 2. It can be seen there that they differ systematically from one another: the means differ by 14 per cent. Therefore, a direct comparison of a sample of ellipticities calculated in this fashion to our predictions (equation 4) is not possible.

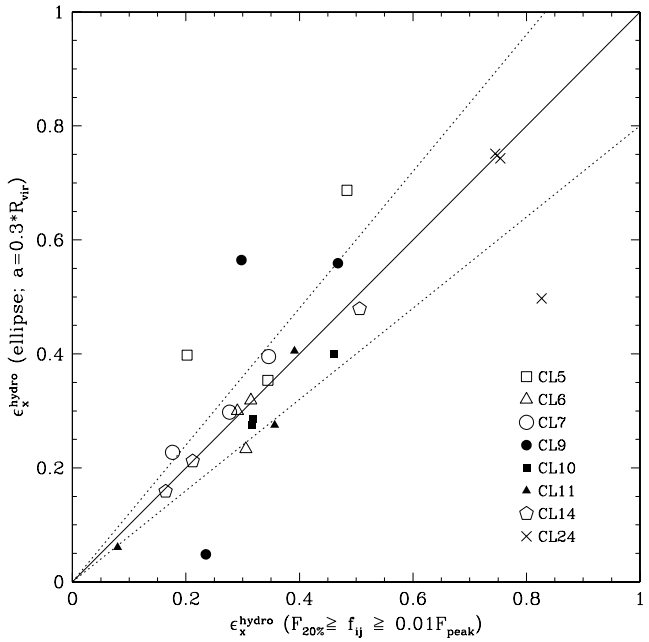

Figure 4. Comparison of ellipticities calculated directly from SB maps of the hydrodynamic simulation clusters using different strategies. The abscissa is the same as in Fig. 2. The ordinate is an ellipticity calculated iteratively using *all* pixels within an elliptical aperture of fixed semimajor axis $a = 0.3\ r_{\rm vir}$ (the method of Buote et al, private communication). Within the dotted lines, the ellipticities differ by less than 20 per cent (see text for further discussion).

Also of interest here is the strategy used by Buote, Hart & Humphrey (private communication). They calculate ellipticities using *all* pixels inside a smooth boundary (i.e. the boundary is not determined by flux level), which is determined by applying the method of Carter & Metcalfe (1980) [used without iteration in the studies of McMillan et al. (1989) and Kolokotronis et al. (2001) as explained in Appendix C] iteratively, starting from a circle, until the ellipticity converges within a given accuracy. The semimajor axis is kept fixed. Fig. 4 shows a comparison of ellipticities (all calculated directly from the hydrodynamic simulation maps), calculated using the methodology of Buote et al. (private communication) (ordinate) and McMillan et al. (1989) (abscissa). The ellipticities agree quite well in mean value and dispersion ($P_{\rm KS} = 89$ per cent), despite the fact that the methodology of Buote et al. (private communication) uses all pixels within the elliptical window. Thus, the choice of a smooth boundary (rather than a flux-selected boundary) makes the ellipticity samples to differ in no systematic way, unlike the case of Fig. 3. A comparison of a sample of ellipticities calculated in this way to our predictions (equation 4) is therefore possible.

Finally, we also explore here the reliability of the analytic model to predict the expected ellipticity of millimetre-wave maps of the SZ effect (SZE) in clusters (see e.g. Carlstrom, Holder & Reese 2002), which map the effective temperature decrement of the microwave background due to the hot electron gas (Sunyaev & Zel'dovich 1970). Fig. 5 shows decrement maps for the cluster in Fig. 1, with contours spaced by a factor of 3 (maps for all eight clusters are included as Supplementary Material to the online version of this article). The maps are qualitatively similar to the SB maps, but the effect of changing triaxiality of the DM haloes in the region spanned by the isodecrement contours shown is more readily noted (because the signal is proportional to $\rho_{\rm gas}$ instead of $\rho_{\rm gas}^2$). We show in the upper right corner of each map the ellipticity obtained in the same manner as Fig. 1, but the decrement threshold and the percentage of signal in the pixels are chosen so that the pixels used cover a region of similar size to the corresponding region in Fig. 1.

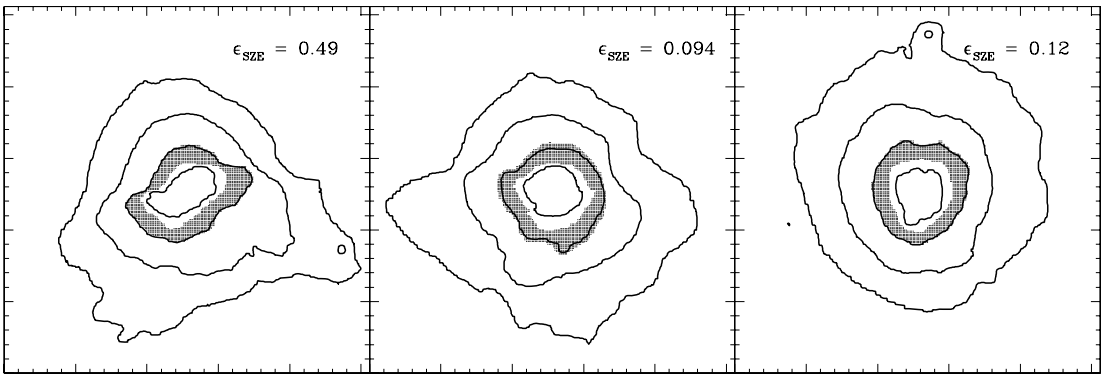

Figure 5. Sample of SZ decrement maps for a hydrodynamic simulation cluster. Each panel presents the map for a LOS along each of the axes of the simulation box. Each square is $2\,h^{-1}$ Mpc across. The solid lines show contours of constant temperature decrement, spaced by factors of 3. The shaded area is the region used to calculate the ellipticity shown in the upper right corners (see text for discussion, and the Supplementary Material section for details of the full figure).

Specifically, the decrement threshold chosen is 10 per cent of the peak decrement in the map (as opposed to the 1 per cent of peak signal in Fig. 1), and the signal in all of the pixels used is 30 per cent of the total signal above the threshold (as opposed to the 20 per cent in Fig. 1). The mean ellipticity and the scatter for this set are $\langle\epsilon_{\rm SZE}\rangle = 0.307 \pm 0.035$ and $\sigma_{\rm SZE} = 0.171 \pm 0.019$, respectively (bootstrap resampling errors). For the set of Fig. 1, but with 10 per cent threshold and 30 per cent flux, $\langle\epsilon_{\rm X}\rangle = 0.359 \pm 0.036$ and $\sigma_{\rm X} = 0.175 \pm 0.033$, respectively (the difference with our 1 per cent threshold and 20 per cent flux prediction above is due to the changing triaxiality of DM haloes). By contrast, the analytic model would predict nearly identical distributions. Thus, although not as successful as for X-ray ellipticities, the analytic model would still be useful to predict, e.g., quantitative trends for ellipticities as a function of cluster redshift.

3 COMPARISON TO CLUSTER-SCALE OBSERVATIONS

Here, we compare our predictions to ellipticity distributions from samples of cluster X-ray observations. We first analyse the methodologies employed by McMillan et al. (1989) and Kolokotronis et al. (2001) to calculate ellipticities for their samples of Abell clusters. We also consider briefly the sample of Mohr et al. (1995) considered by Wang & Fan (2004) for their comparison to observations. These samples use different methodologies to calculate ellipticities, and are affected differently by resolution and noise. Applying a KS test to pairs of samples (all converted to 2D axial ratios), we find that $P_{\rm KS} = 0.0031$ for the McMillan et al. (1989) and Mohr et al. (1995) samples, and $P_{\rm KS} = 0.21$ for the Kolokotronis et al. (2001) and Mohr et al. (1995) samples. This systematic difference between ellipticities calculated by these different methods complicates the comparison of theoretical predictions and observations, but it is usually ignored (e.g. Melott, Chambers & Miller 2001; Wang & Fan 2004). Finally, we analyse a very recent data set from a nearly complete, flux-limited sample of *ROSAT* clusters discussed by Buote et al. (private communication).

Mohr et al. (1995) considered a sample of 51 (mostly Abell) clusters observed by the *Einstein* Imaging Proportional Counter (IPC), for which they obtained a mean 2D axial ratio, η, of $\langle\eta\rangle = 0.80$ and a dispersion $\sigma_\eta = 0.12$. Converting their axial ratios to ellipticities, $\epsilon = 1 - \eta^2$, we obtain $\langle\epsilon\rangle = 0.358 \pm 0.026$ and $\sigma_\epsilon = 0.182 \pm 0.017$. The mean and scatter differ by about 1.5 and 2.5 standard deviations, respectively, from our predictions (equation 4). However, the method of Mohr et al. (1995) uses all pixels above a signal-to-noise ratio level, and therefore gives substantially more weight to the central regions of a SB map, where mergers can significantly affect the ellipticity. Given our discussion of the results presented in Fig. 3, the difference in mean ellipticity (10 per cent) is entirely within the expectation given the different strategy. The agreement is somewhat surprising, however, given the potential effect that cooling within clusters could have on the DM haloes (Kazantzidis et al. 2004; Springel et al. 2004). We discuss this further below.

The Kolokotronis et al. (2001) sample consists of 22 *ROSAT* clusters, with a range of velocity dispersions of 400–1000 km s^{-1}. Converting their ellipticities to $\epsilon = 1 - \eta^2$, the mean and dispersion of their sample are $\langle\epsilon\rangle = 0.458 \pm 0.051$ and $\sigma_\epsilon = 0.237 \pm 0.023$. The poor agreement with our prediction (equation 4) is not surprising given that their method emphasizes the cluster centre and there are three clusters in the observational sample showing strong evidence of an ongoing merger: A2804, A2933 and A3128 are all bimodal (Kolokotronis et al. 2001). We have tested that this is indeed the problem by computing ellipticities for the sample of hydroclusters discussed in Section 2, following exactly the procedure of Kolokotronis et al. (2001), which first defines a flux threshold equal to the mean flux within a $600\,h^{-1}$ kpc radius, and then uses all pixels above the threshold. A KS test between the hydrosample of ellipticities calculated this way, and the sample of Kolokotronis et al. (2001), gives $P_{\rm KS} = 0.82$ (the hydrosample is slightly rounder on average). Thus, we conclude that their sample is in agreement with the expectations for a ΛCDM universe.

We have also made a comparison with the *Einstein* data of McMillan et al. (1989) consisting of 49 clusters. Here, we can expect the comparison to be a better test on the cosmological sample because they explicitly exclude image centres, thus their shape statistic is less sensitive to mergers (see Appendix C). However, the mean and dispersion of their sample are $\langle\epsilon\rangle = 0.240 \pm 0.020$ and $\sigma_\epsilon = 0.142 \pm 0.015$. There is poor agreement with our prediction (equation 4) for the mean this time. It appears unlikely that this discrepancy could be entirely due to missing physics (e.g. cooling) in the simulations we have used to test the analytic model described in Appendix A. We note that even after excluding the three bimodal clusters from the Kolokotronis et al. (2001) sample, a KS test against the McMillan et al. (1989) sample (once ellipticities are converted to the same definition in terms of flux-moment eigenvalues; see Appendix C) rejects that they are compatible at the 96 per cent CL.

The coarser angular resolution of the *Einstein* data probably contributes to this disagreement. For example, we find that if we smooth the X-ray map of the ΛCDM cluster we discuss in Appendix C (see Fig. C1) with a Gaussian window of $80\,h^{-1}$ kpc [FWHM, roughly corresponding to the 1.6 arcmin resolution of the McMillan et al. (1989) data at the median redshift of their sample, $z = 0.057$], the X-ray ellipticities can change significantly: the entry in Column 6 of Table C1 would be 0.40 (0.23, 0.46) for the x-axis (y-axis, z-axis) as compared to 0.43 (0.28, 0.51) without smoothing. This is also consistent with the changes found by Buote & Canizares (1996) for five clusters with *Einstein*, later analysed with *ROSAT* data. We find that a 20 per cent change in the predicted ellipticities would make them marginally compatible with the data.

A more important contribution to the difference with our predictions seems to be the effect of noise. Many clusters in the McMillan et al. (1989) sample have very small ellipticities but do not look round at all. We find a similar result for the simulated clusters when noise is introduced at a level close to the threshold (1 per cent of peak flux) used for the calculation of $\epsilon_{\rm X}$. For example, for a cluster for which the ellipticity without smoothing and noise is $\epsilon_{\rm X} = 0.18$, with smoothing and noise (the latter making the largest difference) $\epsilon_{\rm X} = 0.08$. If we put this level of noise in all the hydroclusters, we find that the hydrosample becomes fully compatible with the McMillan et al. (1989) sample: $P_{\rm KS} = 0.87$. Thus, our predictions do not appear to be incompatible with this data sample.

Finally, we discuss the recent sample of ellipticities obtained by Buote et al. (private communication) for the flux-limited sample of *ROSAT* clusters of Reiprich & Böhringer (2002). As we showed in Section 2.2 and Fig. 4, a direct comparison to our predictions (equation 4) in this case is possible. It is worth emphasizing here that an important advantage of these data is that all the ellipticities are calculated within the *same* aperture ($0.3r_{\rm vir}$). The mean and dispersion for the sample of Buote et al. (private communication) are $\langle\epsilon_{\rm X}\rangle = 0.376 \pm 0.019$ and $\sigma_\epsilon = 0.122 \pm 0.014$, respectively ($\epsilon = 1 - \eta^2$). The dispersion is less than expected, but only by approximately 1σ. However, the mean is substantially larger than expected (by approximately 2.8σ). This appears to be due to the expected mass dependence of axial ratios.

As discussed in Paper I, dark matter haloes are systematically more triaxial the larger their mass. A simple relation was found that describes this behaviour: $\langle s \rangle = 0.54(M_*/M_{\rm vir})^{0.05}$ (see Paper I). Many of the clusters in the sample discussed by Buote et al. (private communication) are much more massive than the sample of simulation clusters we used to make our predictions (equation 4). This is to be expected because the observational sample was flux limited and, therefore, massive clusters are overrepresented (relative to a volume-limited sample, which the simulation clusters represent). Using the scaling relation above, we find that our prediction for the mean ellipticity of a sample of clusters with a mass function like that of the clusters analysed by Buote et al. (private communication) would be $\langle \epsilon_{\rm X} \rangle = 0.353 \pm 0.013$ (instead of equation 4).[1] The remaining difference could well be a statistical fluctuation, given that the intrinsic dispersion in ellipticities is $\sigma_\epsilon \sim 0.14$. Thus, we can expect fluctuations $O(\sigma_\epsilon/\sqrt{N}) = 0.022$ for a sample of the size of the Buote et al. (private communication) sample.

As we explained in Section 1, our scaling of mean axial ratio $\langle s \rangle$ with mass is based on simulations spanning a wide range of masses. If we assume the milder scaling advocated by JS, $\langle s \rangle = 0.54(M_*/M_{\rm vir})^{0.03}$, based on simulations covering a narrower range of masses, the predicted mean ellipticity would be $\langle \epsilon_{\rm X} \rangle = 0.312 \pm 0.011$ instead, which is 3.4σ lower than the observations. It is also worth pointing out that the data themselves show evidence of mass dependence, although not at a high level of confidence. If we split the data of Buote et al. (private communication) by mass, for clusters below (above) $M_{\rm vir} = 10^{15}\, h^{-1}\, {\rm M}_\odot$ $\langle \epsilon_{\rm X} \rangle = 0.357 \pm 0.027$ and $\sigma_\epsilon = 0.117 \pm 0.020$ ($\langle \epsilon_{\rm X} \rangle = 0.393 \pm 0.026$ and $\sigma_\epsilon = 0.123 \pm 0.019$). There are about equal number of clusters in each subsample. Although the difference in mean value is not highly significant, it is of the magnitude expected (10 per cent) using the scaling of Paper I.

We conclude from the comparison with these four data samples that the predictions for cluster X-ray shapes in the ΛCDM cosmology, *assuming gas cooling has only a small effect on the shape of their dark matter haloes*, are in good agreement with the data. A more stringent test, however, would require a larger sample of clusters and a better quantitative understanding of the effect of cooling.

We have attempted to estimate quantitatively the effect of gas cooling on cluster X-ray ellipticities, which generically makes DM haloes less triaxial. We use a hydrodynamic simulation of one cluster for which cooling and star formation were abruptly terminated at redshift $z = 2$ in order for the cluster to have reasonable star and gas fractions (see Kazantzidis et al. 2004). The effect of cooling on DM halo axial ratios for this cluster agrees very well with the *average* effect shown in Fig. 4 of Springel et al. (2004). We calculated the short/long axial ratio in logarithmic radial distance bins in order to directly compare to the figure in Springel et al. (2004). We find that there is good agreement in the distance range (0.1–0.3) $r_{\rm vir}$. Therefore, we have estimated the expected effect on X-ray ellipticities in two ways. We can compute the change in ellipticity by comparing the ellipticities with and without cooling for this one cluster. Since the change in axial ratios seems to be representative of the expected average change, we can estimate that the effect would be to make X-ray ellipticities 10–20 per cent smaller. We have also estimated the effect by generating a catalogue of DM 'haloes', where a halo is represented as a set of axial ratios and a concentration. We generate axial ratios using the form of the distribution of s and q found in simulations (we use $\bar{s} = 0.54$ and $\sigma_{\rm s} = 0.1$ for the Gaussian distribution of s; Paper I). We generate concentrations using the lognormal distribution of Wechsler et al. (2002), with mean of 7 and a log-dispersion of 0.14. Finally, we orient randomly the principal axes in a box. A mean short/long axial ratio $\bar{s} = 0.54$ instead of $\bar{s} = 0.45$ adequately represents the effect seen on average by Springel et al. (2004), and the effect on the cluster discussed here. We find in this case that we can expect X-ray ellipticities to be ∼25 per cent smaller. It is thus rather surprising that we find such good agreement with the data *without* taking the effects of cooling into account.

We also note here that the average ellipticity of the Buote et al. (private communication) clusters slightly *decreases* with radius: $\langle \epsilon_{\rm X} \rangle = 0.404 \pm 0.028$ ($\langle \epsilon_{\rm X} \rangle = 0.395 \pm 0.024$, $\langle \epsilon_{\rm X} \rangle = 0.378 \pm 0.022$) within a 300 (500, 700) kpc aperture ($H_0 = 70$ km s^{-1} Mpc^{-1}; 37 clusters have data over this radial range). The trend is weak (the data are consistent with no radial dependence), but consistent with our predictions if we take into account the scaling of axial ratios with radius that we have found in our *dissipationless* simulations (Paper I): we would have expected $\langle \epsilon_{\rm X} \rangle$ to increase by about 6 per cent from the largest to the smallest aperture. The trend, however, is opposite to that expected from the simulations that include cooling and star formation (Kazantzidis et al. 2004; Springel et al. 2004), which predict dark matter haloes to be rounder at smaller radii than at larger radii. We estimate, by generating catalogues, that $\langle \epsilon_{\rm X} \rangle$ would be expected to decrease by at least 6 per cent in that case.

We have considered a lower σ_8 cosmology, in which DM haloes are predicted to be more triaxial (see Paper I), as a possible explanation of this surprising result. If DM haloes were more triaxial, the predicted X-ray ellipticities would increase and then cooling could bring results into agreement with the data. We have found in Paper I that a simple scaling relation accounts for the dependence of axial ratios on σ_8 (see Paper I, equation 7). The predicted $\bar{s}$ can then be used as above to generate a catalogue of axial ratios. We find that even for a value of σ_8 as low as $\sigma_8 = 0.75$ [as favoured by the *Wilkinson Microwave Anisotropy Probe* (*WMAP*) 3-yr results paper by Spergel et al. (2006)], the expected mean X-ray ellipticity of a sample like the Buote et al. (private communication) sample changes only to $\langle \epsilon_{\rm X} \rangle = 0.378 \pm 0.013$ (from $\langle \epsilon_{\rm X} \rangle = 0.353 \pm 0.013$ for $\sigma_8 = 0.9$). If in addition we lower the matter density to $\Omega_{\rm m} = 0.24$ (Spergel et al. 2006), the mean ellipticity increases only by 2 per cent.

There are potential biases that can affect comparisons of the model with observations. For example, in relaxed cooling flow clusters the temperature decreases toward the centre in the cluster core (e.g. De Grandi & Molendi 2002; Vikhlinin et al. 2005). Line emission of low-temperature X-ray gas can significantly alter the $\rho_{\rm gas}^2\sqrt{T}$ weighting assumed in our analysis and, therefore, the shape of the X-ray brightness isophotes. To take this effect into account, however, we need to know the temperature and metallicity distribution in clusters. However, Buote et al. (private communication) have calculated ellipticities in annuli as well, i.e. excluding the cluster centres altogether. The mean ellipticity is only slightly (4 per cent) higher.

Another possible source of bias can arise in comparisons with the shape estimates based on the isophotes defined at a constant fraction of the peak flux of the cluster. The profiles of real clusters are often quite 'cuspy' in their centres (e.g. Vikhlinin et al. 2006) and are considerably steeper than the radial gas density profiles of clusters in our adiabatic simulations. This difference in the radial gas distribution will result in different radii of the isophotes defined with respect to the peak flux. This may mean that the shapes would be

[1] We do the calculation by generating a Monte Carlo set, picking the observationally estimated mass of a cluster, and using the scaling relation above to get a corresponding $\langle s \rangle$. We then draw axial ratios for the cluster using the form of the distribution of s and q found in simulations (see Paper I).

measured at systematically different radii in simulations and observations (smaller radius in observations). Note, however, that Buote et al. (private communication) calculate ellipticities within the same aperture, as we have stressed above.

Two qualitative trends in X-ray maps appear to reflect the more complex nature of dark matter haloes seen in high-resolution simulations. Buote & Canizares (1996, and references therein) have pioneered detailed studies of X-ray maps to constrain cluster halo profiles. They studied five Abell clusters using oblate and prolate spheroids in order to bracket the possibilities, and concluded that the ellipticity (there is only one axial ratio if one assumes oblate and prolate spheroids) of the haloes was constrained to be in the range 0.40–0.55. The systematic trend of interest here is that four of the five clusters show a decreasing ellipticity of the X-ray isophotes at larger radii. A similar trend can be seen in the gas data for the two high-resolution adiabatic simulation clusters discussed in Appendix C (see Figs C1 and C2) and is due to the decreasing triaxiality of the dark matter halo at a larger radius. The effect is not very pronounced, so the simple isothermal/homeoidal halo model could still be used for the ellipticity comparison above. The same is not true, however, for SZ decrement maps (see Fig. C3). As discussed in Appendix C, the different sensitivity of SZ maps to density and temperature ($\propto \int \rho_{\rm gas} T$) makes these observations more sensitive to our simplistic assumptions, and the simple mapping from halo shape parameters will break down more visibly. More detailed modelling will likely be required to interpret SZ shape measurements accurately.

A second complication of interest here was noted by McMillan et al. (1989), who pointed out that a fraction ($\sim$15 per cent) of their clusters exhibited isophotal twist with a 'continuous rotation of the intermediate isophotes'. We have found that one of the high-resolution simulation clusters discussed in Appendix C (see Fig. C2) shows this kind of twist due to coherent twist of the dark matter density shells. Of course, it will be interesting to quantify the frequency of this effect, as well as its origins. The degree of misalignment in the case of this cluster [$\sim 45^\circ$ in the radial range $\sim(0.3–1)r_{\rm vir}$] would be rare judging by the results of JS for 12 haloes. However, a direct comparison is not possible because the angles involved are not the same.

Therefore, while some observational quantities are somewhat insensitive to the complex non-homeoidal nature of halo structure, many observed properties are quite sensitive to changing ellipticities and twists. Specifically, the higher order trends in halo shapes may leave imprints in cluster gas that could be studied in detail by analyses of X-ray and SZ maps.

Cluster X-ray ellipticities can be expected to evolve with redshift due to increased halo triaxiality (see Paper I, and references therein). Recent papers have called attention to a possible significant evolution of the ellipticity with redshift even over the nearby redshift range $z = 0$–0.1 (Melott et al. 2001; Plionis 2002), and have claimed that cluster X-ray and optical profiles are a little less flattened than predicted by dissipationless and hydrodynamic simulations (see Floor et al. 2003, 2004, and references therein). However, it is important to compare observational data to simulated clusters of similar mass (the Floor et al. clusters were more massive than most of the observed clusters) and, as we have explained (see Appendix C), to mimic the way the data were treated. It is hard to draw clear conclusions when the rather different McMillan et al. (1989) and Kolokotronis et al. (2001) X-ray data sets and analyses are combined, as was done by Melott et al. (2001). Jeltema et al. (2005) have detected evolution in cluster morphology in a more homogeneous sample of clusters with *Chandra* data. However, the morphology is not quantified as an ellipticity, therefore we cannot assess how well this observation constrains theory in this paper.

4 CONCLUSIONS

We have presented a simple analytic model to predict cluster halo gas profiles based on dark halo shapes, under the assumption that clusters are isothermal and in hydrostatic equilibrium within haloes that are homeoidal ellipsoids (i.e. with constant axial ratios). We have tested this analytic model against high-resolution hydrodynamical simulations of clusters and found that samples of ellipticities of X-ray maps can be adequately described by this model. Therefore, we used the model to calculate the expected properties (mean and scatter) of the distribution of ellipticities of X-ray clusters in the ΛCDM cosmology. In comparing these predictions with observations, we were careful to calculate the predicted ellipticity using the same method used to analyse the X-ray data. This is important, since each analysis used a different method, and we showed that some of these methods were less robust than others against noise, resolution and confusion by observational artefacts. We also included the mass dependence expected in the distribution of ellipticities due to dependence of DM halo shape on mass, which we had accurately characterized using a large suite of dissipationless simulations in Paper I.

Our main conclusion is that the predicted distribution of ellipticities in the ΛCDM cosmology, neglecting gas cooling, is in good agreement with observational samples of ellipticities for galaxy clusters. The agreement with the recent Buote et al. (private communication) analysis of a complete *ROSAT* sample is especially significant because it is a large and statistically well-defined sample that has been analysed using a method that robustly measures ellipticity. The measured ellipticity is $\langle \epsilon_{\rm X} \rangle = 0.376 \pm 0.019$. Our predicted ellipticity for this sample, analysed the same way, is $\langle \epsilon_{\rm X} \rangle = 0.353 \pm 0.013$ with the cosmological parameter $\sigma_8 = 0.90$, and $\langle \epsilon_{\rm X} \rangle = 0.378 \pm 0.013$ with $\sigma_8 = 0.75$; both predictions are in agreement with the observations. Earlier cluster shape measurements by McMillan et al. (1989) from *Einstein* data were less significant because of poor resolution and the effects of noise, although we showed that the method used by these authors would work well with better data. The ellipticity calculated from *ROSAT* cluster data by Kolokotronis et al. (2001) emphasized the cluster centres more than would be optimal, although it too is consistent with our theoretical predictions when this is taken into account.

The agreement between X-ray data on cluster shapes and ΛCDM predictions that do not include gas cooling might at the first sight seem surprising, since part of the cluster gas certainly does cool and form stars. However, the cluster simulations with cooling (Kazantzidis et al. 2004; Springel et al. 2004) indicate that the cluster centres are significantly less elliptical than the X-ray data imply. This is true even when the cooling was stopped artificially at redshift $z = 2$ (Kazantzidis et al. 2004), in order to prevent much more gas from cooling and forming stars than occurs in real clusters (the 'overcooling' problem), because even in this case much of the cooling and star formation occur near the cluster centre. There are other indications that additional heat is needed in cluster centres to prevent the gas from becoming thermally unstable (the 'cooling-flow' problem), and plausible sources are AGN energy input (e.g. Begelman & Ruszkowski 2005; Heinz et al. 2006) and/or conduction (e.g. Zakamska & Narayan 2003). However, neither AGN energy input nor conduction was included in the simulations with cooling which predicts cluster ellipticity lower than observed. It will be interesting

to see whether simulations that include such effects will predict cluster shapes in better accord with observations.

The shape of dark matter haloes undoubtedly cannot be fully characterized by simple models with constant axis ratios, such as our analytic model. We have used inertia tensor derived axial ratios to characterize halo shapes in a simple way, and explored how simple assumptions about halo shapes can be used to compare to observational tracers of halo structure. While we find that this simple approach is adequate for comparison with cluster X-ray shapes, we find that more detailed predictions will be required for other observational comparisons (Appendix C). For example, the isothermal/homeoidal assumption becomes less useful for comparison to measurements like SZ decrement maps. In addition, radially decreasing ellipticities can arise from the changing shape of isodensity contours with radius, and twists in X-ray isophotes can arise from misalignment of isodensity contours at large and small radius. Predictions aimed at that kind of data will require a more detailed analysis of ΛCDM halo shapes, including a detailed characterization of ellipticities as a function of radius, and the frequency of isophotal twists. Work in this direction is under way.

ACKNOWLEDGMENTS

We thank Daisuke Nagai and Andrew Zentner for their help. We also thank the anonymous referee for comments that helped to clarify our discussion. JSB was supported by NSF grant AST-0507816 and by startup funds at UC Irvine. AVK was supported by the NSF under grants AST-0206216 and AST-0239759, and by NASA through grant NAG5-13274. BA and JRP were supported by AST-0205944 and NAG5-12326. The numerical simulations used in this study were performed at the National Centre for Supercomputing Applications (NCSA, Urbana-Champaign). This research has made use of NASA's Astrophysics Data System Bibliographic Services.

REFERENCES

Allgood B., Flores R. A., Primack J. R., Kravtsov A. V., Wechsler R. H., Faltenbacher A., Bullock J. S., 2006, MNRAS, 367, 1781 (Paper I)
Avila-Reese V., Firmani C., Klypin A. A., Kravtsov A. V., 1999, MNRAS, 310, 527
Barnes J., Efstathiou G., 1987, ApJ, 319, 575
Begelman M. C., Ruszkowski M., 2005, Phil. Trans. R. Soc. A, 363, 655
Binney J., 1985, MNRAS, 212, 767
Bryan G. L., Norman M., 1998, ApJ, 495, 80
Bullock J. S., 2002, in Natarajan P., ed., Proc. Yale Cosmology Workshop, The Shapes of Galaxies and Their Dark Matter Haloes. World Scientific, Singapore, p. 109
Buote D. A., Canizares C. R., 1996, ApJ, 457, 565
Buote D. A., Tsai J. C., 1995, ApJ, 439, 29
Carlstrom J. E., Holder G. P., Reese E. D., 2002, ARA&A, 40, 643
Carter D., Metcalfe N., 1980, MNRAS, 191, 325
Chandrasekhar S., 1969, Ellipsoidal Figures of Equilibrium. Yale Univ. Press, New Haven, CT
De Grandi S., Molendi S., 2002, ApJ, 567, 163
Dubinski J., Carlberg R. G., 1991, ApJ, 378, 496
Fabian A. C., 2003, in Avila-Reese V., Firmani C., Frenk C. S., Allen C., eds, Rev. Mex. Astron. Astrofis. Ser. Conf. Vol. 17, Galaxy Evolution: Theory & Observations. UNAM, Mexico, p. 303
Floor S. N., Melott A. L., Miller C. J., Bryan G. L., 2003, ApJ, 591, 741
Floor S. N., Melott A. L., Motl P. M., 2004, ApJ, 611, 153
Frenk C., White S. D. M., Davis M., Efstathiou G., 1988, ApJ, 327, 507
Heinz S., Brüggen M., Young A., Levesque E., 2006, MNRAS, 373, L65
Hernquist L., 1990, ApJ, 356, 359
Jeltema T. E., Canizares C. R., Bautz M. W., Buote D. A., 2005, ApJ, 624, 606
Jing Y. P., Suto Y., 2002, ApJ, 574, 538 (JS)
Jing Y. P., Mo H. J., Borner G., Fang L. Z., 1995, MNRAS, 276, 417
Kasun S. F., Evrard A. E., 2005, ApJ, 629, 781
Kazantzidis S., Kravtsov A. V., Zentner A. R., Allgood B., Nagai D., Moore B., 2004, ApJ, 611, L73
Kolokotronis V., Basilakos S., Plionis M., Georgantopoulos I., 2001, MNRAS, 320, 49
Kravtsov A. V., Klypin A., Hoffman Y., 2002, ApJ, 571, 563
Lee J., Suto Y., 2003, ApJ, 585, 151
McMillan S. L. W., Kowalski M. P., Ulmer M. P., 1989, ApJS, 70, 723
Melott A. L., Chambers S. W., Miller C. J., 2001, ApJ, 559, L75
Mohr J. J., Evrard A. E., Fabricant D. G., Geller M. J., 1995, ApJ, 447, 8
Nagai D., Kravtsov A. V., 2003, ApJ, 587, 514
Navarro J. F., Frenk C. S., White S. D. M., 1996, ApJ, 462, 563
Plionis M., 2002, ApJ, 572, L67
Reiprich H. T., Böhringer H., 2002, ApJ, 567, 716
Rosati P., Borgani S., Norman C., 2002, ARA&A, 40, 539
Spergel D. N. et al., 2006, preprint (astro-ph/0603449)
Springel V., White S. D. M., Hernquist L., 2004, in Ryder S. D., Pisano D. J., Walker M. A., Freeman K. C., eds, IAU Symp. 220, Dark Matter in Galaxies. Astron. Soc. Pac., San Francisco, p. 421
Sunyaev R. A., Zel'dovich Ya. B., 1970, Comments Astrophys. Space Phys., 2, 66
Suwa T., Habe A., Yoshikawa T., Okamoto T., 2003, ApJ, 588, 7
Thomas P. A. et al., 1998, MNRAS, 296, 1061
Thomas P. A., Muanwong O., Pearce F. R., Couchman H. M. P., Edge A. C., Jenkins A., Onuora A., 2001, MNRAS, 324, 450
Vikhlinin A., Markevitch M., Murray S. S., Jones C., Forman W., Van Speybroeck L., 2005, ApJ, 628, 655
Vikhlinin A., Kravtsov A. V., Forman W., Jones C., Markevitch M., Murray S. S., Van Speybroeck L., 2006, ApJ, 640, 691
Wang Y.-G., Fan Z.-H., 2004, ApJ, 617, 847
Warren M. S., Quinn P. J., Salmon J. K., Zurek W. H., 1992, ApJ, 399, 405
Wechsler R. H., Bullock J. S., Primack J. R., Kravtsov A. V., Dekel A., 2002, ApJ, 568, 52
Zakamska N. L., Narayan R., 2003, ApJ, 582, 162

APPENDIX A: GAS DENSITY INSIDE TRIAXIAL HALOES

Here, we present a simple model of the gas density expected inside a cluster halo and use it to calculate X-ray properties such as SB. The model can also be used for other gas-density-dependent observations, such as SZE maps from millimetre-wave observations of clusters (see e.g. Carlstrom et al. 2002). We define the dark matter halo density model, and calculate its potential, in Appendix B. The gas density model is based on three common approximations about the gas:

(1) the gas is in hydrostatic equilibrium,
(2) the gas is isothermal and
(3) the gas makes a negligible contribution to the total mass.

These assumptions are quite restrictive, although it is trivial to modify equation (A1) for a polytropic gas. In Appendix C, we will relax all of the assumptions and work directly with the gas in two high-resolution simulations of galaxy clusters. We work out expected X-ray properties for the clusters in the simulations and compare them with the predictions based on the model described here. We find that the model works fairly well, despite its simplifying assumptions. We further test the model statistically against a small sample of high-resolution simulation clusters in Section 2.

With the assumptions listed above, the gas density expected at a point (x, y, z) inside a triaxial halo can be written in terms of the gas

density at the origin, the dark matter potential $\Phi(x, y, z)$ and the gas temperature T. For the halo density model discussed in Appendix B, we find it convenient to work with the potential in units of the overall factor $4\pi G s q \rho_s R_s^2$. Therefore, we write

$$\rho_{\rm gas}(x, y, z) = \rho_{\rm gas}(0) \exp\{-\Gamma[\tilde{\Phi}(x, y, z) - \tilde{\Phi}(0)]\}. \quad \text{(A1)}$$

Here, $\tilde{\Phi}(x, y, z) = \Phi(x, y, z)/4\pi G s q \rho_s R_s^2$, so the constant Γ is given by

$$\Gamma = 4\pi G s q \rho_s R_s^2 \frac{\mu m_p}{k T}, \quad \text{(A2)}$$

where μ is the mean molecular weight. For clusters with galaxy velocity dispersion σ, $kT \sim \mu m_p \sigma^2$ (see e.g. Rosati et al. 2002). Therefore, since $4\pi s q \rho_s R_s^2 = {\rm O}(\sigma^2/G)\, c_{\rm vir}$ (see Section 2), we can expect $\Gamma \sim c_{\rm vir}$.[2]

We can use this simple model to calculate the expected X-ray SB of hot gas in a dark halo with a given potential. Since we have assumed the gas is isothermal, SB $\propto \int \rho_{\rm gas}^2$, where the integral is calculated along the LOS. In Appendix B, we calculate the potential $\Phi(x, y, z)$ in the principal-axis coordinate system of the dark matter halo. Therefore, in order to calculate SB we need the orientation of the LOS in this coordinate system. We use the conventions of Binney (1985), in which the LOS-axis is defined by azimuthal and polar angles ϕ and θ, respectively.

We thus have the following model to predict the X-ray SB map expected for a given projection of a dark matter halo in a simulation box. We first calculate the axial ratios $s < q < 1$ by the iterative procedure described in Section 2; in Appendix C we find that axial ratios calculated using a solid ellipsoid of semimajor axis $0.5 r_{\rm vir}$ works well to predict flux-weighted ellipticities. We also obtain from the procedure the orientation (ϕ and θ) of a given LOS, and the orientation [position angle (PA)] of the projection of the shortest axis of the halo on the plane perpendicular to the LOS. For a given point along the LOS, we find $\rho_{\rm gas}$ by first rotating its coordinates in the plane by the PA. We then apply the inverse of the rotation parametrized by ϕ and θ (Binney 1985). This gives us the coordinates of the point along the LOS in the principal-axis system, from which we obtain $\rho_{\rm gas}$ using equation (A1). Therefore, we can calculate $\int \rho_{\rm gas}^2$ numerically at any given point on the plane. We will refer to this model for the SB as the 'analytic model' (even though it involves numerical integration) in order to distinguish its predictions from those we work out directly from the gas density in two high-resolution simulations of galaxy clusters that we analyse in Appendix C, where we compare predictions for X-ray ellipticities.

APPENDIX B: ANALYTIC POTENTIAL OF TRIAXIAL GENERALIZED NFW HALOES

Here, we consider the potential of triaxial dark matter haloes with a density profile that is a simple generalization of a special case of the spherical profile introduced by Hernquist (1990). We assume that isodensity shells are homeoidal ellipsoids, i.e. with constant axial ratios s and q ($s < q < 1$), and that the density profile is given by

$$\rho(x, y, z) = \frac{\rho_s}{(R/R_s)^\alpha (1 + R/R_s)^{\eta-\alpha}}$$
$$R = \sqrt{x^2 + y^2/q^2 + z^2/s^2}, \quad \text{(B1)}$$

where ρ_s and R_s are a scale density and radius, respectively. Assuming constant axial ratios allows us to reduce the calculation of the potential to a 1D integral, which in some cases can be solved analytically, after a simple transformation of the general result for ellipsoidal mass distributions (Chandrasekhar 1969).

We first consider $\eta = 3$. This was found to be a good approximation (assuming constant axial ratios) by JS for their 12 high-resolution haloes. We also find this to be a good approximation for the haloes of two high-resolution hydrodynamical simulations we discuss in Appendix C. However, since spherical fits to large samples of haloes find deviations from this value (Avila-Reese et al. 1999; Thomas et al. 2001), we also generalize the results to other values below.

The potential of a thin homeoid of mass M (axes $a > b > c$) at a point (x, y, z) outside the shell can be written as (Chandrasekhar 1969)

$$\Phi_M(x, y, z) = -\frac{GM}{2} \int_\lambda^\infty \frac{du}{\sqrt{(a^2+u)(b^2+u)(c^2+u)}}. \quad \text{(B2)}$$

The parameter λ in equation (B2) is the parameter of the confocal ellipse passing through (x, y, z); it is the largest root of

$$\frac{x^2}{a^2+\lambda} + \frac{y^2}{b^2+\lambda} + \frac{z^2}{c^2+\lambda} = 1. \quad \text{(B3)}$$

Since the integral (B2) can be solved analytically, we find that

$$\Phi_M(x, y, z) = -\frac{GM}{\sqrt{a^2-c^2}} \,\text{EllipticF}\left(\sqrt{\frac{a^2-c^2}{a^2+\lambda}}, \sqrt{\frac{a^2-b^2}{a^2-c^2}}\right). \quad \text{(B4)}$$

The potential inside the homeoid is a constant (Chandrasekhar 1969), therefore it is given by $\Phi_M(x, y, z)$ with $\lambda = 0$.

We can construct the potential inside a triaxial NFW-type halo now, assuming homeoidal symmetry (i.e. constant axial ratios). First, for the potential at (x, y, z) due to all mass shells inside (i.e. inside the shell passing through the point), we find

$$\Phi_{\rm in} = -A\,\zeta^{2-\alpha} \int_0^1 {\rm d}m \, \frac{m^{1-\alpha}}{(1+m\zeta)^{3-\alpha}} \times \text{EllipticF}\left(\sqrt{\frac{1-s^2}{1+\lambda(m)/m^2R^2}}, \sqrt{\frac{1-q^2}{1-s^2}}\right). \quad \text{(B5)}$$

Here, $\zeta = R/R_s$, $A = 4\pi G s q \rho_s R_s^2/\sqrt{1-s^2}$ and $\lambda(m)$ is the largest root of

$$\frac{x^2}{m^2R^2+\lambda} + \frac{y^2}{m^2R^2q^2+\lambda} + \frac{z^2}{m^2R^2s^2+\lambda} = 1. \quad \text{(B6)}$$

Second, for the potential due to all shells outside we find

$$\Phi_{\rm out} = -\frac{A}{2-\alpha} \,\text{EllipticF}\left(\sqrt{1-s^2}, \sqrt{\frac{1-q^2}{1-s^2}}\right) \times \left[1 - \left(\frac{\zeta}{1+\zeta}\right)^{2-\alpha}\right]. \quad \text{(B7)}$$

[2] For example, for the SCDM (ΛCDM) cluster discussed in Appendix C, $GM_{\rm vir}/r_{\rm vir} f(c_{\rm vir}) = 1063$ (630) km s^{-1}. The dispersion inside the relevant projected radius ($400\,h^{-1}$ kpc) for these clusters is similar to these values. For the SCDM cluster, the dispersion is $\sigma = 1116$ km s^{-1} (1077 km s^{-1}, 1000 km s^{-1}) along the x-axis (y-axis, z-axis). For the ΛCDM cluster, we find $\sigma = 661$ km s^{-1} (928 km s^{-1}, 650 km s^{-1}). The higher σ along the y-axis is due to a merger nearly along this axis; however, the same Γ chosen to fit the radial fall-off in SB in the plane perpendicular to the x-axis works well for the other two axes.

The total potential is then $\Phi(x, y, z) = \Phi_{\rm in} + \Phi_{\rm out}$. Also, we find that the only change needed for $\eta \neq 3$ is to replace $(1 + m\zeta)^{3-\alpha}$ by $(1 + m\zeta)^{\eta-\alpha}$ in equation (B5), and to replace $(1 - (\zeta/(1 + \zeta))^{2-\alpha})$ in equation (B7) by

$$\frac{(2-\alpha)\,\Gamma(2-\alpha)\,\Gamma(\eta-2)}{\Gamma(\eta-\alpha)} - \frac{\zeta^{2-\alpha}\,\mathrm{hypergeom}([1,\ \eta-\alpha],\ [3-\alpha],\ \zeta/(1+\zeta))}{(1+\zeta)^{\eta-\alpha}}. \quad \text{(B8)}$$

For spherical symmetry ($q = s = 1$), we can check the standard result for the potential of a NFW halo. We can use EllipticF $(x, 1) = x + \mathrm{O}\,(x^3)$ to get

$$\frac{1}{\sqrt{1-s^2}}\,\mathrm{EllipticF}\left(\sqrt{\frac{1-s^2}{1+\lambda(m)/m^2R^2}},\ \sqrt{\frac{1-q^2}{1-s^2}}\right) = \frac{1}{\sqrt{1+\lambda(m)/m^2R^2}}. \quad \text{(B9)}$$

In this case ($q = s = 1$), the right-hand side is just m, and for the NFW profile ($\alpha = 1$, $\eta = 3$) we have

$$\int_0^1 \frac{m\,dm}{(1+m\,\zeta)^2} = \frac{\ln(1+\zeta)+\ln(1+\zeta)\,\zeta-\zeta}{\zeta^2\,(1+\zeta)}. \quad \text{(B10)}$$

Therefore, at radial distance $r = \sqrt{x^2 + y^2 + z^2}$

$$\Phi_{\rm in}(r) = -4\pi G\,\rho_{\rm s}\,{R_{\rm s}}^2\left[\frac{\ln(1+r/R_{\rm s})}{r/R_{\rm s}} - \frac{1}{1+r/R_{\rm s}}\right]$$
$$\Phi_{\rm out}(r) = -4\pi G\,\rho_{\rm s}\,{R_{\rm s}}^2\left(1 - \frac{r/R_{\rm s}}{1+r/R_{\rm s}}\right) \quad \text{(B11)}$$

and the total potential takes the standard form,

$$\Phi(r) = -4\,\pi\,G\,\rho_{\rm s}\,{R_{\rm s}}^2\,\frac{\ln(1+r/R_{\rm s})}{r/R_{\rm s}}. \quad \text{(B12)}$$

For $\alpha \neq 1$ and $\eta \neq 3$, the integral in equation (B5) can be obtained analytically. The spherical potential of a generalized NFW halo is then

$$\Phi(r) = -4\,\pi\,G\,\rho_{\rm s}\,{R_{\rm s}}^2\left\{\frac{\Gamma(2-\alpha)\,\Gamma(\eta-2)}{\Gamma(\eta-\alpha)} + \frac{(r/R_{\rm s})^{2-\alpha}\,\Delta(r/R_{\rm s})}{(2-\alpha)(1+r/R_{\rm s})^{\eta-\alpha}}\right\}, \quad \text{(B13)}$$

where

$$\Delta(x) = \frac{2-\alpha}{3-\alpha}\,\mathrm{hypergeom}\left([1,\eta-\alpha],[4-\alpha],\frac{x}{1+x}\right) - \mathrm{hypergeom}\left([1,\eta-\alpha],[3-\alpha],\frac{x}{1+x}\right). \quad \text{(B14)}$$

APPENDIX C: A COMPARISON OF X-RAY ELLIPTICITY MEASURES

Here, we evaluate the reliability of our method for predicting individual cluster X-ray ellipticities based on the calculated axial ratios of dark matter haloes. Using a hydrodynamical simulation (with cooling) of a single cluster, Buote & Tsai (1995) found that this method, assuming isothermal gas, allows an accurate estimation of the ellipticity of the dark matter even if the gas has a strong temperature gradient, so long as any substructure in the cluster is excluded in the analysis. We use high-resolution *adiabatic* hydrodynamical simulations of two clusters in order to calculate X-ray SB maps directly from the gas data of the simulations. We then compare these maps in detail to predictions based on the properties of their dark matter haloes, using the theoretical model described in Appendix A. We find that the theoretical model can work relatively well (predicting ellipticities within 10 per cent of the gas-data values) depending on exactly how the observational ellipticity is defined. A statistical (rather than case by case) test of the model is presented in Section 2.

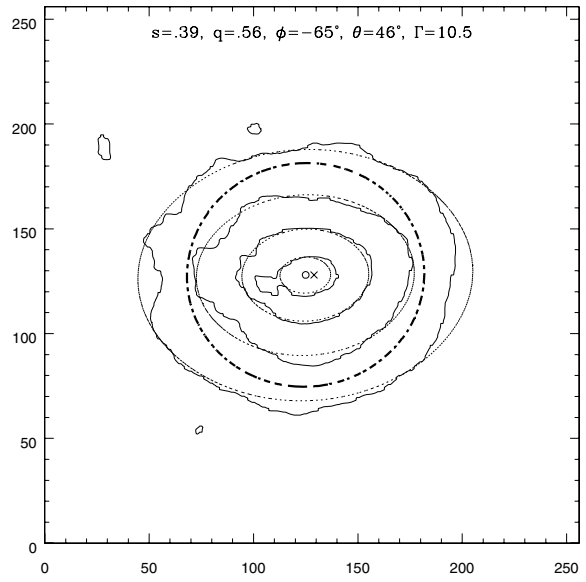

Figure C1. SB plot for the ΛCDM cluster in the yz-plane of the simulation box. The axes are in pixels ($7.8\,h^{-1}$ kpc per pixel) and the solid lines show contours of constant $\int \rho_{\rm gas}^2$, spaced by factors of 10. The SB peak (centroid) is indicated by the cross (open circle), and the innermost solid contour corresponds to a level of 15 per cent of peak value. The dotted-line contours show the predictions of the analytic model described in Appendix A. The factor Γ is estimated by fitting, for one projection, the radial SB profile of the simulation. It is then used for all other projections. Finally, the dashed-line contour illustrates a predicted contour if a more global measure of triaxiality were used (see the text for further discussion).

We first discuss a ΛCDM cluster that has been studied in detail by Nagai & Kravtsov (2003). In Fig. C1, we show a 'SB' map calculated from the gas data of the simulation. The solid lines really show contours of constant value of $\int \rho_{\rm gas}^2$, where the integration is along a LOS parallel to the x-axis of the simulation box. Of course, SB $\propto \int \rho_{\rm gas}^2\sqrt{T}$, but we have dropped the temperature dependence for simplicity, given that it makes only a small difference in calculated ellipticities ($\lesssim$5 per cent). We calculate SB for a given 'pixel' by summing over all cells along the LOS. Coordinates are shown in pixels, with $7.8\,h^{-1}$ kpc per pixel. The dotted line contours are the SB contours predicted by the model described in Appendix A with the factor Γ chosen to match the radial SB profile, $\Gamma = 10.5$. For this halo $c_{\rm vir} = 11.5$, therefore $\Gamma \sim c_{\rm vir}$, as expected (see Section 2). The X-ray ellipticities discussed here are only mildly dependent on Γ [e.g. $\epsilon_{\rm X}^{\rm model} = 0.46$ in Table C1 changes to $\epsilon_{\rm X}^{\rm model} = 0.40(0.48)$ for $\Gamma = 8(13)$]. They are mostly sensitive to the axial ratios s and q, and the relative orientation of the LOS, described by polar angles ϕ and θ in the principal-axis coordinate system. The axial ratios and polar angles were calculated inside an ellipsoid of semimajor axis $600\,h^{-1}$ kpc using the iterative method described in the text, and are shown at the top of the figure. The dashed-line contour illustrates a predicted isophotal contour based on axial ratios calculated with the prescription of Kasun & Evrard (2005). The result is very similar for SZ isodecrement contours.

Table C1. Ellipticity results for ΛCDM cluster (see Fig. C1). Here $\epsilon_X = 1 - \Lambda_-^2/\Lambda_+^2$.

LOS	ϵ_X^{gas} > 0.01	ϵ_X^{model} > 0.01	ϵ_X^{gas} > 0.1	ϵ_X^{model} > 0.1	ϵ_X^{gas} 0.01–0.08	ϵ_X^{model} 0.01–0.08	ϵ_X^{gas} 0.1–0.2	ϵ_X^{model} 0.1–0.2
x-axis	0.61	0.48	0.79	0.49	0.43	0.46	0.72	0.53
y-axis	0.24	0.23	0.40	0.24	0.28	0.23	0.32	0.26
z-axis	0.65	0.51	0.77	0.53	0.51	0.50	0.69	0.48

The highly irregular, innermost solid contour is due to a minor merger nearly in the 'plane of the sky' (about 25° off the *y*-axis of the box). The merger is ideal to test quantitatively observational strategies to calculate an ellipticity that best represents the global triaxiality of the dark matter halo. It is also an ideal test of the reliability of our method because it allows us to gauge what bias can be introduced in the calculation of ellipticities by the presence of a minor merger, which can be expected to be common for cluster-size systems. We discuss both of these issues below.

There are various strategies to calculate X-ray ellipticities. Here, we consider the method used by Kolokotronis et al. (2001) (22 clusters; *ROSAT* data) and McMillan et al. (1989) (49 clusters; *Einstein* data) as examples used in the analyses of samples of clusters. Both studies use the method of Carter & Metcalfe (1980) adapted to an X-ray image. The ellipticity is calculated from the positive roots Λ_+ and $\Lambda_-(\Lambda_+ > \Lambda_-)$ of the characteristic equation

$$(\mu_{20} - \Lambda^2)(\mu_{02} - \Lambda^2) = \mu_{11}^2. \tag{C1}$$

The moments μ_{mn} are defined in terms of the flux f_{ij} at a given pixel (x_i, y_j) by

$$\mu_{mn} = \sum_{ij} f_{ij}(x_i - \bar{x})^m (y_j - \bar{y})^n \Big/ \sum_{ij} f_{ij}, \tag{C2}$$

where $(\bar{x},\bar{y})$ is the image centroid ($\bar{x} = \sum_{ij} x_i f_{ij} / \sum_{ij} f_{ij}$, $\bar{y} = \sum_{ij} y_j f_{ij} / \sum_{ij} f_{ij}$). The ellipticity is then calculated as

$$\epsilon_X = 1 - \Lambda_-^2/\Lambda_+^2 \tag{C3}$$

by McMillan et al. (1989), and as

$$\epsilon_X = 1 - \Lambda_-/\Lambda_+ \tag{C4}$$

by Kolokotronis et al. (2001). We will use equation (C3) here, except when comparing directly with the data of Kolokotronis et al. (2001).

The X-ray ellipticity ϵ_X is rather sensitive to what pixels are used to calculate it. Kolokotronis et al. (2001) use all pixels above a flux threshold (which is the average flux within a region of given radius). For example, in Fig. C1 this threshold is ∼0.01 of the peak flux within $600\,h^{-1}$ kpc (which is the largest radius they use to define the threshold). In Table C1 (Columns 2–5), we show results for the cluster of Fig. C1 for two flux thresholds (0.01 and 0.1 of the peak flux) and for a LOS along each of the axes of the simulation box. This choice of pixels emphasizes the brightness peaks and, therefore, is more sensitive to mergers. Thus, the analytic model prediction for the ellipticity, ϵ_X^{model}, deviates significantly from the value calculated directly from the gas, ϵ_X^{gas}, except when the merger is nearly along the LOS. On the other hand, McMillan et al. (1989) explicitly exclude the centre of an image in order to characterize the global dynamics of a cluster. They use all the pixels containing 20 per cent of the flux above a faint threshold. The latter varies substantially across the sample, but for 80 per cent of clusters it is ∼0.01–0.2 of the peak flux. In Table C1 (Columns 6–9), we show results for two flux ranges (0.01–0.08 and 0.1–0.2) and for a LOS along each of the axes. In this case, the analytic model performs much better, provided the fainter threshold is chosen low enough. If we calculate the deviation of the model ellipticity from the gas ellipticity (using a flux threshold of 0.01) for 100 random LOS, we find the following:

(1) For the McMillan et al. (1989) ellipticity, the analytic model works fairly well; 2/3 of the time the model predicts the ellipticity within 10 per cent of the gas value. Also, it would not bias a statistical sample because it predicts larger and smaller values with equal frequency.

(2) For the Kolokotronis et al. (2001) ellipticity, the analytic model predicts a systematically smaller value. This is expected in this case because the model misses the merger, therefore it predicts rounder SB contours from all viewing angles. In this case, we find that 2/3 of the time the value is 20–30 per cent smaller.

We find similar trends for the mean and the dispersion of ellipticities calculated for the sample of clusters discussed in Section 2, although individual values can deviate more than indicated here.

The flux level at the outermost contour in Fig. C1 is ∼0.002 of the peak flux. At this flux level, the contour is clearly rounder than the model prediction (due to the fact that the dark matter halo gets rounder farther out, whereas the analytic model assumes constant axial ratios). However, pixels up to much higher flux levels (∼0.06 of peak flux) enter the calculation in order to accumulate 20 per cent of the flux above this fainter threshold in the approach of McMillan et al. (1989). For example, for the *x*-axis $\epsilon_X^{gas} = 0.41$ and $\epsilon_X^{model} = 0.45$ in the flux range 0.002–0.06 of peak flux. Therefore, the model works well down to lower thresholds.

The analytic model assumes that the gas is isothermal in order to predict the SB. We can check how much this is likely to affect a comparison with actual data by calculating the ellipticity from the simulation data including the temperature dependence. We find that for the flux levels considered here, the effect is rather small. For example, the entry in Column 2 of Table C1 would be 0.59 (0.23, 0.63) for the *x*-axis (*y*-axis, *z*-axis) as compared to 0.61 (0.24, 0.65) assuming isothermality. The temperature in this cluster falls by a factor of ∼1.9 in the radial range $(0.1–0.5)r_{vir}$, which is consistent with observations (see De Grandi & Molendi 2002, and references therein). Therefore, the temperature variation of the simulation gas is representative of that of real clusters.

We have also tested whether using the dark matter potential of this cluster would directly significantly improve the prediction for ϵ_X. The assumptions are still the same, but the potential is calculated directly from the dark matter distribution in order to predict the gas density. We find that the results improve as follows. For example, the entry in Column 3 of Table C1 would be 0.53 (0.25, 0.55) for the *x*-axis (*y*-axis, *z*-axis) instead of 0.48 (0.23, 0.51).

Finally, in order to study whether the analytic model indeed performs better in the absence of a merger, we have analysed in the same

Table C2. Ellipticity results for SCDM cluster (see Fig. C2). Here $\epsilon_{\rm X} = 1 - \Lambda_-^2/\Lambda_+^2$.

LOS	$\epsilon_{\rm X}^{\rm gas}$ > 0.01	$\epsilon_{\rm X}^{\rm model}$ > 0.01	$\epsilon_{\rm X}^{\rm gas}$ > 0.1	$\epsilon_{\rm X}^{\rm model}$ > 0.1	$\epsilon_{\rm X}^{\rm gas}$ 0.01–0.09	$\epsilon_{\rm X}^{\rm model}$ 0.01–0.09	$\epsilon_{\rm X}^{\rm gas}$ 0.1–0.2	$\epsilon_{\rm X}^{\rm model}$ 0.1–0.2
x-axis	0.30	0.35	0.38	0.38	0.25	0.34	0.38	0.34
y-axis	0.48	0.37	0.45	0.42	0.51	0.35	0.42	0.39
z-axis	0.48	0.55	0.52	0.56	0.44	0.54	0.48	0.55

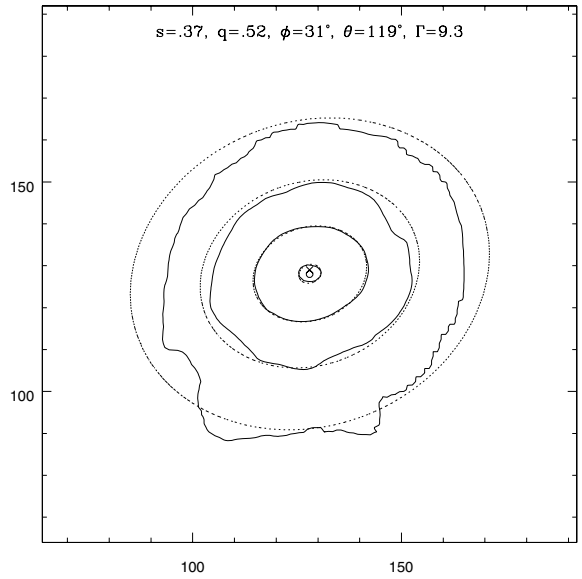

Figure C2. SB plot for the SCDM cluster in the yz-plane of the simulation box. The axes are in pixels ($15.6\,h^{-1}$ kpc per pixel) and the meaning of symbols is as in Fig. C1. In this case, the innermost solid contour corresponds to a level of 25 per cent of peak value, and each solid contour is drawn at one-tenth of the solid-contour levels of Fig. C1.

manner a high-resolution simulation cluster that does not have an ongoing merger. It is a SCDM cluster discussed in detail by Kravtsov et al. (2002). In Fig. C2, we show the SB map calculated as in Fig. C1, and in Table C2 we show the results for the ellipticity. For this cluster $\Gamma = 9.3$ and $c_{\rm vir} = 10.4$, therefore $\Gamma \sim c_{\rm vir}$ as before. In this case, the model works reasonably well for either one of the definitions of ellipticity, provided that the flux threshold is sufficiently high. For faint thresholds, the model fails to reproduce the trend of rounder and twisted SB contours in the simulation (for LOS = y-axis, the reverse trend in Table C2 is due to the chance projection of a distant hot spot that appears only at a level $\sim$0.01 of peak flux). It is in fact the twisted SB contours that cause most of the difference between model and simulation gas. This is due to the fact that isodensity shells are fairly misaligned in this case. The projected, $100\,h^{-1}$ kpc-thick isodensity shell of $400\,h^{-1}$ kpc (800–$900\,h^{-1}$ kpc, 1000–$1050\,h^{-1}$ kpc) semimajor axis makes a 15° (35°, 60°) angle with the vertical direction in Fig. C2. Such large misalignments were found to be rare by JS, therefore we assume here that the model also works down to the faint threshold level of $\sim$0.01 of peak flux in the absence of a merger, and for both ellipticities.

In Section 3, we analyse the expected distribution of X-ray ellipticities for cluster-mass haloes in the cosmological box discussed in Section 2. We calculate ellipticities using the analytic model, and compare the distribution to the data of McMillan et al. (1989) and Kolokotronis et al. (2001).

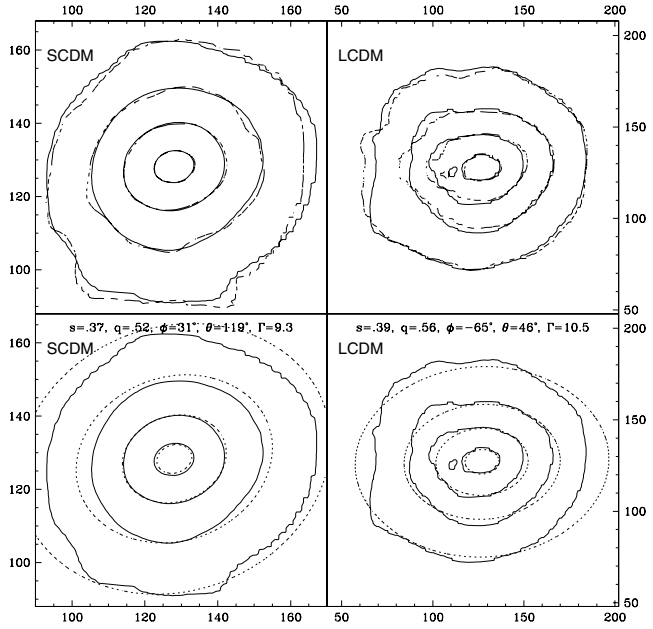

Figure C3. Temperature decrement map for the two clusters of Figs C1 and C2 in the yz-plane of the corresponding simulation boxes. The axes are in pixels, and each box is $1.25\,h^{-1}$ Mpc across. The solid lines show contours of constant $\int \rho_{\rm gas}\,T$, spaced by factors of 3. The innermost solid contour corresponds to a level of 60 per cent (50 per cent) of peak value for the SCDM (ΛCDM) cluster. The top panels compare the shape of the contours of constant $\int \rho_{\rm gas}$ (dashed lines) to the decrement-level contours. The bottom panels compare the prediction of the analytic model for $\int \rho_{\rm gas}$ (dotted lines) with the decrement-level contours (see the text for further discussion).

We have also considered the reliability of the analytic model to predict the shape of SZE maps of clusters. In Fig. C3, we show 'temperature decrement' maps for the two clusters we have discussed. The solid lines show contours of constant value of $\int \rho_{\rm gas}\,T$ (spaced by factors of 3). The integration is along a LOS parallel to the x-axis of the corresponding simulation box, as was the case in Figs C1 and C2. Since the dependence on gas temperature is linear in this case, we can expect a more significant effect of temperature on the shape of isodecrement contours. The top panels of Fig. C3 compare the shape of the contours of constant value of $\int \rho_{\rm gas}$ only (dashed lines) to decrement contours.[3] Both sets of solid contours are calculated directly from the gas and temperature data of the corresponding simulation. It can be seen that in the presence of a merger (the ΛCDM cluster case), the temperature dependence indeed makes

[3] The dashed-line contours are not shown spaced by a fixed factor. The levels are just chosen to give contours of similar size to the solid contours, in order to compare shapes at a given radial distance.

the isodecrement contours notably different from contours of $\int \rho_{\rm gas}$. However, in the absence of a merger (the SCDM cluster case) they agree fairly well in shape. For example, the ellipticity $\epsilon_{\rm SZE} = 1 - \Lambda_-^2/\Lambda_+^2$, calculated using the signal between the second and third contours, is $\epsilon_{\rm SZE} = 0.20$ (0.24) for the SCDM (ΛCDM) cluster. The ellipticities calculated using the gas density alone are 0.21 and 0.36, respectively. Thus, analytic models to calculate $\epsilon_{\rm SZE}$ assuming isothermal gas will err by a large margin in the presence of a merger, *even if* $\epsilon_{\rm SZE}$ *is calculated outside the core region*. This is unlike what we have found for X-ray ellipticities.

Furthermore, even in the absence of a merger, the changing triaxiality of the dark matter halo makes model predictions for ellipticity in the SZ maps miss the values $\epsilon_{\rm SZE}$ by a larger margin than in the case of X-ray ellipticity. The bottom panels of Fig. C3 show the predictions of the analytic model for $\int \rho_{\rm gas}$ (dotted lines) compared to the 'isodecrement contours' of the top panels (solid lines). It can be seen there that, even in the absence of a merger (left-hand side), the ellipticity of the analytic model contours is too large (even if compared to the simulation-data contours for $\int \rho_{\rm gas}$ only (dashed lines of top panels). For example, the ellipticity between the second and third contours of the analytic model predictions is 0.33 (0.46) for the SCDM (ΛCDM) cluster. We find similar results for the other LOS. Thus, reliable predictions (i.e. within 10 per cent of gas-data values) for ellipticity in SZE maps need to incorporate the changing triaxiality of the dark matter haloes. However, the model is still useful to predict statistics of cluster samples such as the mean and dispersion (see Section 2).

SUPPLEMENTARY MATERIAL

The following supplementary material is available for this article.

Figure 1. X-ray SB maps for hydrodynamic simulation clusters. Each row presents the SB for a LOS along each of the axes of the simulation box. Each square is $2\,h^{-1}$ Mpc across. The solid lines show contours of constant SB, spaced by factors of 10. The shaded area is the region used to calculate the ellipticity shown in the upper right corners.

Figure 5. SZ decrement maps for a hydrodynamic simulation cluster. Each panel presents the map for a LOS along each of the axes of the simulation box. Each square is $2\,h^{-1}$ Mpc across. The solid lines show contours of constant temperature decrement, spaced by factors of 3. The shaded area is the region used to calculate the ellipticity shown in the upper right corners.

This material is available as part of the online paper from: http://www.blackwell-synergy.com/doi/abs/10.1111/j.1365-2966.2007.11658.x (this link will take you to the article abstract).

Please note: Blackwell Publishing are not responsible for the content or functionality of any supplementary materials supplied by the authors. Any queries (other than missing material) should be directed to the corresponding author for the article.

This paper has been typeset from a TEX/LATEX file prepared by the author.